Journal of Colloid and Interface Science 579 (2020) 607–618

Contents lists available at ScienceDirect

Journal of Colloid and Interface Science

journal homepage: www.elsevier.com/locate/jcis

Preparation of CoS_2 supported flower-like NiFe layered double hydroxides nanospheres for high-performance supercapacitors

Jinmi Tian [a,1], Aitang Zhang [a,1], Rui Liu [a], Weiguo Huang [a], Zhen Yuan [b,*], Rongkun Zheng [b], Di Wei [b], Jingquan Liu [a,b,*]

[a] College of Materials Science and Engineering, Institute for Graphene Applied Technology Innovation, Collaborative Innovation Centre for Marine Biomass Fibers, Materials and Textiles of Shandong Province, Qingdao University, Qingdao 266071, China
[b] College of Material Science and Engineering, Linyi University, Linyi 276000, Shandong, China

HIGHLIGHTS

- The sample were designed and prepared through the facile hydrothermal process.
- The NiFe-LDH@CoS_2@Ni electrode exhibits a high capacity of 11.28 F cm^{-2} (3880 F g^{-1}) at a current density of 2 mA cm^{-2} (1.17 A g^{-1}).
- When the NiFe-LDH@CoS_2@Ni fabricated as an ASC device, it can light up a blue LED for 30 min.

GRAPHICAL ABSTRACT

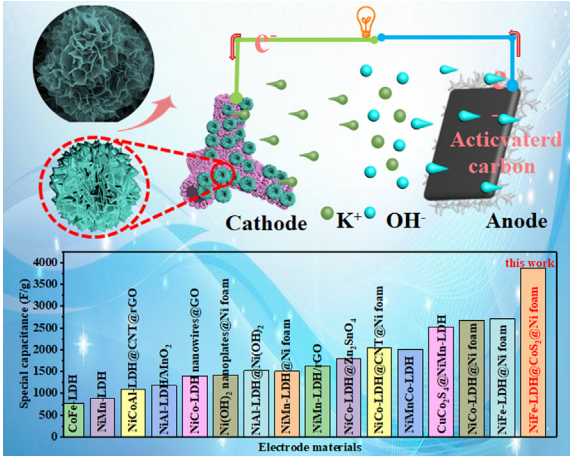

ARTICLE INFO

Article history:
Received 18 April 2020
Revised 13 June 2020
Accepted 21 June 2020
Available online 26 June 2020

Keywords:
CoS_2 nanosheets
NiFe layered double hydroxides nanospheres
Supercapacitor

ABSTRACT

Layered double hydroxides (LDHs) are a kind of classic pseudocapacitive materials with lamellar structure and large specific surface area, which have attracted swinging attention in the electrochemical energy storage area. The CoS_2@Ni is synthesized through a hydrothermal process, followed by surface generation of the flower-like nickel-iron layered double hydroxide (NiFe-LDH) nanospheres through a hydrothermal process, which is directly used to design a binder-free electrode with a splendid capacitance capability. The as-synthesized NiFe-LDH@CoS_2@Ni electrode presents an outstanding specific capacitance of 11.28 F cm^{-2} (3880 F g^{-1}) at 2 mA cm^{-2} (1.17 A g^{-1}) in a three electrodes system. Also, the all-solid-state asymmetric supercapacitor (ASC) is combined utilizing the NiFe-LDH@CoS_2@Ni hybrid as the positive electrodes and active carbon covered Ni foam as negative electrodes, respectively. The as-fabricated ASC exhibits a high energy density of 15.84 Wh kg^{-1} at the power density of 375.16 W kg^{-1} and can be able to lighten a blue LED indicator for more than 30 min, revealing that the prepared NiFe-LDH@CoS_2@Ni owns great potential in the aspect of practical applications. Therefore, the prepared

* Corresponding authors at: College of Materials Science and Engineering, Institute for Graphene Applied Technology Innovation, Collaborative Innovation Centre for Marine Biomass Fibers, Materials and Textiles of Shandong Province, Qingdao University, Qingdao 266071, China (J. Liu).
E-mail addresses: yuanzhen@lyu.edu.cn (Z. Yuan), jliu@qdu.edu.cn (J. Liu).
[1] Jinmi Tian and Aitang Zhang contributed equally to this work.

https://doi.org/10.1016/j.jcis.2020.06.086

NiFe-LDH@CoS_2@Ni with outstanding electrochemical properties could be applied for high-performance supercapacitors.

1. Introduction

With the rapidly increasing consumption of energy, it is greatly imperative to search for sustainable energy sources and facilitate energy storage to satisfy the future requirement of a low-carbon and sustainable economy [1–4]. Environmentally friendly electronic energy storage devices, such as supercapacitors (SCs), have drawn extensive concern [5,6]. SCs have been enormously investigated on account of their low cost, high power density, cycling stability and fast charge/discharge ability [7]. Generally, SCs consist of two categories mainly electrical double-layer capacitors (EDLCs) and pseudocapacitors, which are divided by their working principles [8]. The EDLCs are categorized on account of charges diffusion and accumulation on the boundary surface of the electrode/electrolyte [9]. For EDLCs, carbon materials such as carbon nanosheets [10], carbon nanowires and reduced graphene oxide [11] are usually used for electrode materials owing to their remarkable cycling stability. However, carbon-based materials usually suffer from a series of drawbacks such as the uncontrollable pore size and shape, long ion-diffusion distance which makes the accumulation of charge in the electrical double layer limited, leading to poor specific capacitances of EDLCs [12]. While pseudocapacitors primarily take advantage of fast and reversible faradaic redox reaction to store energy, hence they could provide more excellent specific capacitance than EDLCs [13]. Transition metal oxides/hydroxides, conducting polymers and layer double hydroxides are promising electrode materials for pseudocapacitors [14].

Recently, nanostructured metal sulfide as one of the novel energy storage materials has attracted great attention on account of their excellent electrical and catalytic properties [15–17]. Cobalt sulfide (CoS_2) has desirable electroconductibility and thermal stability, which can achieve remarkable capacitance property and cycling performance as supercapacitor material [18]. Additionally, layered double hydroxides (LDHs) have attracted widespread concern due to their laminated structures, large surface area and excellent electrochemical properties [19–24]. Therefore, we fabricated the CoS_2 nanosheets coated flower-like NiFe-LDH nanospheres directly on the surface of 3D nickel foam substrate for high-performance supercapacitors. Meanwhile, layered double hydroxides (LDHs) have attracted widespread concern due to their laminated structure, regularly low cost of raw materials, environmentally friendly and large specific surface area [25,26]. Various materials with different morphologies (such as nanoparticles [27], nanorods [28], nanowires [29], nanotubes [30], and flower-like [31]) have been synthesized and served as electrode materials in energy storage devices. Actually, powdered LDHs are prepared through hydrothermal or co-precipitation processes which generally required polymer binders (such as Nafion) to form compact electrodes, resulting in poor electrical conductivity and weak stability. To overcome these limitations, great efforts have been devoted to rational project and composition of hybrid nanocomposites with different hierarchical structures and morphologies, especially in the form of hierarchical nanosheets directly grown on 3D conductive substrates to enhance the electrical conductivity and consequently improve the electrochemical properties [32]. For example, Ni foam supported the flower-like MnO_2@NF/NiFe LDHs nanosheets prepared and made use of electrode material for supercapacitor, which demonstrated high specific capacitance (4274.4 mF cm^{-2} at 5 mA cm^{-2}), outstanding cycling stability and high energy density (24.6 mWh cm^{-2} at 350 mW cm^{-2}) [31]. Xing et al. reported the direct generation of NiCo-LDH nanosheets on 3D Ni foam with a facile hydrothermal method, which showed an ultrahigh capacitance of 2617 F g^{-1} at 1 A g^{-1}.

In this work, the CoS_2 nanosheets are densely grown on the surface of Ni foam through the hydrothermal reaction. Subsequently, the as-synthesized CoS_2@Ni was then coated with flower-like NiFe-LDH nanospheres with lamellar structure through another hydrothermal procedure to obtain the NiFe-LDH@CoS_2@Ni. Additionally, the as-prepared hierarchical NiFe-LDH@CoS_2@Ni hybrids were directly utilized to fabricate a binder-free electrode which presented an outstanding capacitive performance owing to the unique flower-like structure. The prepared NiFe-LDH@CoS_2@Ni electrode presents an outstanding capacitance of 11.28 F cm^{-2} (3880 F g^{-1}) at 2 mA cm^{-2} (1.17 A g^{-1}) in the three electrodes system. Furthermore, an all-solid-state asymmetric supercapacitor (ASC) was assembled by applying the as-prepared NiFe-LDH@CoS_2@Ni hybrid as the positive electrodes and active carbon covered Ni foam as the negative electrodes, respectively. The as-fabricated ASC presented a high energy density of 15.84 Wh kg^{-1} at the power density of 375.16 W kg^{-1} and is able to lighten a blue LED indicator for more than 30 min, revealing that the prepared NiFe-LDH@CoS_2@Ni presents great potential for practical applications. Therefore, the prepared NiFe-LDH@CoS_2@Ni with outstanding electrochemical properties should envision potential practical applications in high-performance supercapacitors.

2. Experimental sections

2.1. Materials

Nickel foam was purchased from Shanghai Zhongwei New Material Co., Ltd. Hydrochloric acid, Cobalt (II) nitrate hexahydrate ($Co(NO_3)_2{\cdot}6H_2O$, AR), sodium thiosulfate pentahydrate ($Na_2S_2O_3{\cdot}5H_2O$, AR), nickel(II) nitrate hexahydrate ($Ni(NO_3)_2{\cdot}6H_2O$, AR), iron (III) nitrate hexahydrate ($Fe(NO_3)_3{\cdot}9H_2O$, AR), urea (H_2NCONH_2, AR) ethanol, potassium hydroxide (KOH, AR), acetylene black (AR), polyvinylidene fluoride (PVDF, AR), ethanol (AR) and activated carbon were all purchased from Sinopharm Chemical Reagent Co., Ltd. All chemicals used were of analytical grade and were used as supplied without any further purification.

2.2. Synthesis of the CoS_2 heterostructure on the Ni foam (CoS_2@Ni)

Typically, a piece of nickel foam (1.0 × 1.0 cm^2) was cleaned by sonication in 1.0 M HCl solution for 15 min to remove the surface oxygen complexes and other impurities. Then, the cleaned Ni foam was washed with ultrapure water and ethanol repeatedly, respectively. Thereafter, it was placed in a vacuum oven under 50 °C to be dried adequately for subsequent use. 2.04 g $Co(NO_3)_2{\cdot}6H_2O$ and 6.94 g $Na_2S_2O_3{\cdot}5H_2O$ were dissolved in 70 mL water, the resulting mixture was stirred to obtain a uniform solution. Subsequently, the pretreated Ni foam was immersed in the above-mixed solution and treated in a 100 mL Teflon-lined stainless steel autoclave at 85 °C for 3 h. Later, the resulting product was cleaned with ethanol and ultrapure water repeatedly and dried at 60 °C in a vacuum drying oven to obtain the CoS_2@Ni precursor.

2.3. Generation of flower-like NiFe-LDH nanospheres on CoS_2@Ni precursor. (NiFe-LDH@CoS_2@Ni)

The flower-like structured nickel-iron layered double hydroxide (NiFe-LDH) nanospheres were directly generated on CoS_2@Ni precursor through a one-pot hydrothermal method. Typically, 1 mmol $Ni(NO_3)_2{\cdot}6H_2O$, 4 mmol $Fe(NO_3)_3{\cdot}6H_2O$ and 4 mmol H_2NCONH_2 were dissolved in 60 mL water, the resulting mixture was stirred to obtain a uniform solution. Subsequently, the pretreated CoS_2@-Ni was immersed into the above-mixed solution and treated in a 100 mL teflon-lined stainless-steel autoclave at 120 °C for 10 h. For comparison, NiFe-LDH grown on CoS_2@Ni with different hydrothermal times (5 h and 20 h) was prepared, which were named as NiFe-LDH@CoS_2@Ni-5, NiFe-LDH@CoS_2@Ni-20, respectively. What's more, the NiFe layered double hydroxide directly grown on Ni foam (NiFe-LDH@Ni) was also prepared under the same condition. The resulting product was cleaned with ethanol and ultrapure water repeatedly and dried at 60 °C in a vacuum drying oven to obtain the samples.

2.4. Characterizations

The morphology of the samples and element content was tested by field-emission scanning electron microscopy (SEM) (Model JSM-2010, JEO) equipped with energy-dispersive X-ray spectroscopy (EDS). The chemical structures of the materials were analyzed by transmission electron microscopy (TEM), high-resolution transmission electron microscopy (HRTEM) and X-ray photoelectron spectroscopy (XPS), a Thermo Escalab 250XI spectrometer. The crystal structure was collected by X-ray diffraction (XRD) (Ultima IV X-ray diffractometer, Rigaku, Japan). The Brunauer-Emmett-Teller (BET) surface area by N_2 sorption was measured by a BET surface area analyzer (V-sorb 2800S).

2.5. Fabrication of electrodes and electrochemical measurements

The electrochemical workstation (CHI 760E), made by Shanghai Chenhua Instrument Factory, China, was used to perform the electrochemical measurements at room temperature. In the three-electrode system, the synthesized hybrid (1.0 × 1.0 cm^2) served as the working electrodes directly, the platinum foil was applied as electrodes, and the mercuric oxide electrode was applied as reference electrodes. 6 M KOH aqueous solution was used as the test electrolyte. Cyclic voltammetry (CV) tests were implemented in the voltage range between 0 V and 0.7 V at different scan rates of 10, 20, 30, 40, 50, 60, 70, 80, 90 and 100 mV s^{-1}, respectively. Galvanostatic charge/discharge (GCD) curves were carried out in a potential window from 0 V to 0.45 V at different current densities of 2, 3, 5, 8, 10, 20 and 30 mA cm^{-2} respectively. Additionally, electrical impedance spectroscopy (EIS) measurements were implemented in the frequency response range from 100 Hz to 0.01 kHz with an open circuit potential a 5 mV AC perturbation. The specific capacitance can be calculated by the following equation [33]:

$$C_A = \frac{I\int V\Delta t}{sV^2} \tag{1}$$

where C_A (F cm^{-2}) is the area capacitance, t (s) means the discharge time, s (cm^2) means the electrode's effective area, I (A) and V (V) is the discharge current and the potential window, respectively.

2.6. Fabrication of KOH-based hydrogel electrolyte

Typically, two grams of PVA was dissolved in 20 mL of ultrapure water at 80 °C to form a uniform solution. Then, 10 mL of 6 M KOH solution was added with stirring after cooling solution to about 65 °C to afford the KOH/PVA hydrogel electrolyte for further utilization.

2.7. Fabrication of ASC and electrochemical measurements

Acetylene black, polyvinylidene fluoride and active carbon with a mass ratio of 1: 1: 8 dissolved in ethanol were to design the active carbon (AC) electrode. Acetylene black was used as a conductive agent and PVDF was used as a binder. Then the mixture was dried in a vacuum at 50 °C for 5 h. Afterward, 17.5 mg of the resulting products were embedded into the nickel foam (2.0 × 2.0 cm^2). The ASC device was designed by applying AC and the as-prepared NiFe-LDH@CoS_2@Ni (1.0 × 1.0 cm^2) as the negative electrode and the positive electrode, respectively, while the pre-prepared KOH/PVA hydrogel served as the electrolyte. Typically, as-prepared free-standing NiFe-LDH@CoS_2@Ni and AC coated nickel foam electrodes were attached to Ni films which worked as a current collector. Subsequently, the pre-prepared KOH/PVA gel electrolyte was dropped onto the surface of the NiFe-LDH@CoS_2@Ni and AC coated nickel foam electrodes until saturation. Then the NiFe-LDH@CoS_2@Ni and AC coated nickel foam electrodes were pressed together under little pressure with KOH/PVA gel electrolyte to achieve the NiFe-LDH@CoS_2@Ni//AC ASC device. Here, the PVA worked as both the solid gel electrolyte and a separator simultaneously. Compared to the supercapacitors packed with aqueous electrolytes and a separator, the polymer gel electrolytes of KOH/PVA exhibit excellent safety and stability. To obtain a high electrochemical properties asymmetric supercapacitor, the two electrodes should conform to the relationship of charge balance ($q^+ = q^-$), where q means the charge stored by the electrode, calculated by the following equation:

$$q = C \times m \times \Delta V \tag{2}$$

where C (F g^{-1}) is the specific capacitance, V (V) and m (g) is the mass of the active material and the potential window, respectively. From the equation, the standard mass ratio (m^+/m^-) of electroactive material at the positive and negative electrodes in an ASC can be calculated according to the formula:

$$m^+/m^- = C^-\Delta V^-/C^+\Delta V^+ \tag{3}$$

where C (F g^{-1}) is the specific capacitances of the positive and negative electrodes, V (V) is the voltage range for positive and negative electrodes. The specific capacitance (C_s) of the ASC can be calculated from the galvanostatic charge-discharge curves according to the following equation:

$$C_s = \frac{2I\int V\Delta t}{mV^2} \tag{4}$$

where t (s) is the discharge time, V (V) is the voltage range, m (g) is the total mass of AC electrode, I (A) and V (V) refers to the discharge current and the potential window, respectively.

I (A) is the discharge current, t (s) is the discharge time, V (V) is the voltage range, and m (g) is the total mass of active materials on both electrodes. The energy density E (Wh kg^{-1}) and power density P (W kg^{-1}) can be calculated by the following equations:

$$E = \frac{1}{2}C_s\Delta V^2 \tag{5}$$

$$P = E/\Delta t \tag{6}$$

3. Results and discussions

Flower-like NiFe-LDH nanospheres were directly generated on the CoS_2@Ni nanosheets via hydrothermal strategy, as shown in

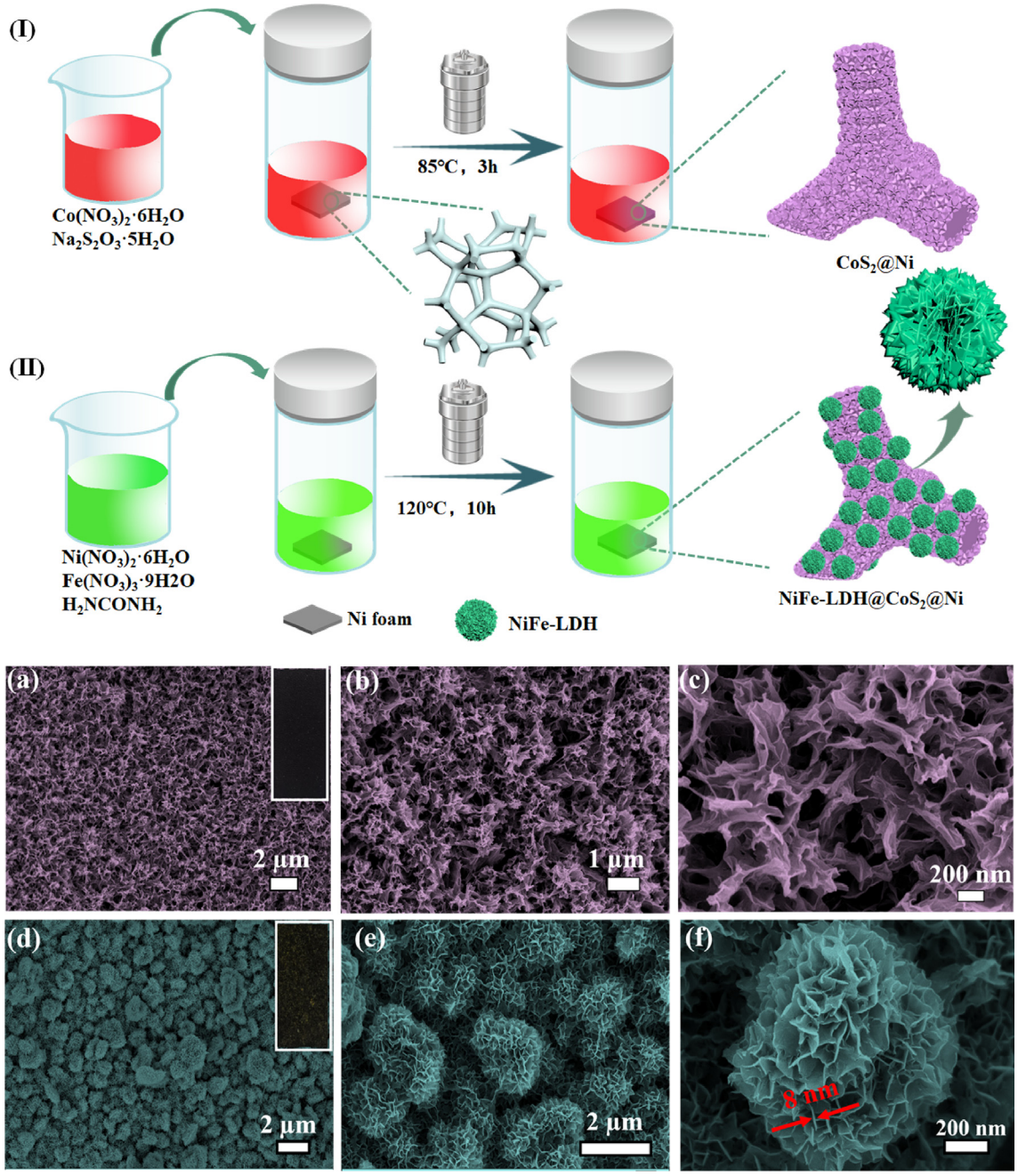

Fig. 1. (I) Schematic illustration for the preparation of CoS_2@Ni nanosheets. (II) Schematic illustration for the synthesis of NiFe-LDH@CoS_2@Ni. Low (a) and high (b-c) magnification SEM images of the CoS_2@Ni nanosheets. Low (d) and high (e-f) magnification SEM images of the NiFe-LDH@CoS_2@Ni flower-like nanospheres.

Fig. 1, where Ni foam was used as the template on account of its 3D porous structure and excellent electronic conductivity. The CoS_2 nanosheets were densely grown on the surface of Ni foam after the hydrothermal process (Step I). During the reaction, $Na_2S_2O_3$ reacts with H_2O to form the intermediate product of H_2S. Subsequently, the Co^{2+} reacted with H_2S to generate cobalt disulfide nanosheets (CoS_2). The reactions involved can be illustrated as follows [34]

$$Na_2S_2O_3 + H_2O \rightarrow Na_2SO_4 + H_2S$$

$$H_2S + H_2O \rightarrow 2\,H_3O^+ + S^{2-}$$

$$CO^{2+} + S^{2-} \rightarrow CoS_2$$

Subsequently, NiFe-LDH nanospheres with the flower-like structures were directly generated on the surface of CoS_2@Ni to obtain NiFe-LDH@CoS_2@Ni (Step II). Before the hydrothermal process, the as-synthesized CoS_2@Ni was soaked in a homogeneous solution containing Ni^{2+}, Fe^{3+}, NO_3^- and urea in Teflon-lined autoclave. As the temperature increased, the OH^- and CO_3^{2-} were produced from the hydrolysis of urea [35,36]. The formation of CO_3^{2-} in the interlamellar of LDHs nanosheets would expand the LDHs layers and reduce their interactions, which has advantages to achieve the LDHs nanosheets with atomical thickness. Moreover, different from the means by adding extra alkali to generate OH^-, the relatively slow liberation of OH^- generated from the hydrolyzed urea could lead to the slow generation and aggregation of

the ion from the primary particles and fast form crystallization of thinner and larger nanosheets [37]. The reactions involved can be illustrated as follows:

$$CO(NH_2)_2 + H_2O \rightarrow 2NH_3 + CO_2$$

$$NH_3 \cdot H_2O \rightarrow NH_4^+ + OH^-$$

$$CO_2 + H_2O \rightarrow CO_3^{2-} + 2H^+$$

$$(1\text{-}x)\ Ni^{2+} + x\ Fe^{3+} + 2\ OH^- \rightarrow (Ni_{1-x}Fe_x)(OH)_2$$

The synthesized nanosheets via a hydrothermal process were first investigated using a scanning electron microscope (SEM). The SEM image of bare Ni foam was shown in Fig. S1, which revealed that the Ni foam surface was highly rough with micrometer-sized pores, which were beneficial to the growth of precursor, demonstrating that Ni foam can be used as a template for surface modification. As shown in Fig. 1a–c, it can be observed that the irregular CoS_2 nanosheets were generated on the macroporous Ni foam substrate. After another hydrothermal process, flower-like NiFe-LDH nanospheres were formed by the thinner NiFe-LDH nanosheets with approximately 10 nm in thickness as shown in Fig. 1d–f. CoS_2 nanosheets provide enormous anchoring sites for the NiFe-LDH nanosheets to grew, subsequently obtain the hybrid composite with flower-like structure.

To investigate the microstructure of NiFe-LDH@CoS_2@Ni and CoS_2@Ni in detail, transmission electron microscope (TEM), high-resolution transmission electron microscope (HRTEM), selected area electron diffraction (SAED), energy dispersive X-ray (EDX) spectrum and element mapping analyses X-ray diffraction (XRD) were carried out. TEM and HRTEM characterized the morphologies and structures of the as-prepared samples. As shown in Fig. 2a, it can be observed that the irregular CoS_2 nanosheets were generated on the macroporous Ni foam substrate. The TEM images of irregular CoS_2 nanosheets are shown in Fig. 2b. The HRTEM image of CoS_2@Ni (shown in Fig. 2c) indicated its high crystallinity. Moreover, as shown in Fig. S2, the SEM image and its corresponding element mapping images of CoS_2@Ni evidenced the existence and uniform distribution of S, Co and Ni elements. Additionally, the chemical composition of the CoS_2@Ni was analyzed by EDX and the results show the elemental ratio of CoS_2@Ni in Fig. S2. Fig. 2e displays the TEM image of NiFe-LDH@CoS_2@Ni with flower structure, which is composed of nanosheets with large specific surface area. This result is in accord with the SEM images as shown in Fig. 2d. The HRTEM image of the sample (Fig. 2f) can be indicated which has a great crystallinity. The interplanar distance of 0.24 nm should be assigned to a typical crystalline structure, corresponding to the (012) plane of the NiFe-LDH phase [38]. As shown in Fig. 2e, the prepared NiFe-LDH flowers have an average diameter of approximately 1 μm. The energy-dispersive X-ray (EDX) spectrum (Fig. 2k) and its corresponding element mapping images (Fig. 2g-j) of NiFe-LDH@CoS_2@Ni evidenced the existence and uniform distribution of S, Ni, Co and Fe elements which confirmed the successful generation of the hierarchical laminated NiFe-LDH@CoS_2@Ni. The EDX spectrum of NiFe-LDH@CoS_2@Ni revealed the atomic contents of Co and Fe are 9.41% and 0.85%, respectively. Furthermore, XRD (Fig. 2l) was applied to check the phase and composition of the NiFe-LDH@CoS_2@Ni, CoS_2@Ni and Ni foam. The three characteristic peaks located at 2θ = 44.50°, 51.85° and 76.37° can be attributed to the (111), (200) and (220) plans of the cubic phase metallic nickel (JCPDS 04-0850) [31,38,39], respectively. The three characteristic peaks located at 2θ = 29.24°, 35.84° and 56.94° should be attributed to the (200), (211) and (311) plans of the cubic phase metallic CoS_2@Ni, respectively. The XRD spectrum of NiFe-LDH@CoS_2@Ni showed three diffraction bands at 2θ = 9.7°, 20.0° and 30.1°, which should be corresponding to the (003), (006) and (012) planes of LDH materials, respectively [40].

Furthermore, X-ray photoelectron spectroscopy (XPS) measurements were implemented to further investigate the different valence states of Co, Fe, Ni and S elements in NiFe-LDH@CoS_2@Ni sample as shown in Fig. 3a–d. The survey spectra of the as-obtained CoS_2@Ni and NiFe-LDH@CoS_2@Ni samples are also shown in Fig. S3a, from which the Co, O, S, Ni and Fe elements can be identified expressly in NiFe-LDH@CoS_2@Ni. XPS measurements were implemented to further investigate the different valence states of Co, Ni and S elements in CoS_2@Ni as shown in Fig. S3. The Co 2p and Ni 2p spectra can be well-fitted with two spin-orbit doublets and two shakeup satellites (marked by "Sat") using a Gaussian fitting method (Fig. 3a, c). The high-resolution Co 2p, Fe 2p, Ni 2p and S 2p spectra of NiFe-LDH@CoS_2@Ni are shown in Fig. 3a–d. As shown in Fig. 3a, the peaks located at around 797.1 eV can be attributed to Co $2p_{1/2}$ and the peaks located at around 781.9 eV and 775.4 eV can be attributed to Co $2p_{3/2}$, respectively, which indicate the co-existence of Co^{3+} and Co^{2+} in the NiFe-LDH@CoS_2@Ni [41]. The Fe $2p_{3/2}$ peaks are located at 707.63 eV and 714.72 eV, and Fe $2p_{1/2}$ peaks are located at 725.17 eV, suggesting the co-existence of Fe^{2+} and Fe^{3+} states (Fig. 3b). The Ni $2p_{3/2}$ at 856.21 eV for Ni^{2+} and Ni $2p_{1/2}$ at 873.92 eV for Ni^{2+} peaks manifest the existence of Ni element. According to these results, the NiFe-LDH@CoS_2@Ni is composed of Ni^{2+}, Ni^{3+} and Fe^{2+}, Fe^{3+} species (Fig. 3c) [42]. The peak located at 162.52 eV is attributed to the binding energy of S $2p_{3/2}$, which may be concerned with the ionic sulfur with low coordination. The peak located at 161.37 eV is attributed to the binding energy of S $2p_{1/2}$, which may be related to the high synergistic interaction between S and NiFe-LDH alloy (Fig. 3d) [43–45].

N_2 adsorption-desorption isotherms were obtained to investigate the porosity of CoS_2@Ni and NiFe-LDH@CoS_2@Ni. As shown in Fig. 3e, the Brunauer-Emmett-Teller (BET) surface area of NiFe-LDH@CoS_2@Ni was significantly improved from 114.84 to 370.75 $m^2\ g^{-1}$ when the CoS_2@Ni precursor was covered with flower-like NiFe-LDH nanospheres. As shown in the inset of Fig. 3f, the pore size distribution of NiFe-LDH@CoS_2@Ni hybrid is mainly located at 4.8 nm. The large specific surface area of NiFe-LDH@CoS_2@Ni should create enormous active sites and ion channels for attaining an outstanding electrochemical performance.

Moreover, to further investigate the evolution process for the synthesis of hierarchical NiFe-LDH@CoS_2@Ni, the experiments of NiFe-LDH prepared with different growth times are carried out and the corresponding SEM images are shown in Fig. 4. The processes reveal the morphological and structural transformation from messy random nanosheets into the flower-like heterostructure. NiFe-LDH wrinkly nanosheets grown on the CoS_2@Ni precursor were observed after 5 h hydrothermal treatment, which exhibited a wrinkled morphology (NiFe-LDH@CoS_2@Ni-5). After 10 h, the NiFe-LDH began to aggregate to form the flower-like structure (NiFe-LDH@CoS_2@Ni). However, the flower-like structures were gradually destroyed after 20 h (NiFe-LDH@CoS_2@Ni-20). Also, TEM images and N_2 adsorption-desorption isotherms, as well as their pore size distributions of NiFe-LDH@CoS2@Ni-5 and NiFe-LDH@CoS2@Ni-20, are shown in Fig. S4. As shown in Fig. S4a and b, the NiFe-LDH nanosheets grown on the CoS_2@Ni precursor were observed after 5 h hydrothermal treatment, which exhibited a wrinkled morphology. However, the flower-like structure was gradually destroyed after 20 h as shown in Fig. 4. The Brunauer-Emmett-Teller (BET) measurements for the NiFe-LDH@CoS_2@Ni-5 and NiFe-LDH@CoS_2@Ni-20 samples have been carried out and the surface areas were measured to be 22.65 $m^2\ g^{-1}$ and 52.12 $m^2\ g^{-1}$, respectively. In addition, the NiFe-LDH@CoS_2@Ni showed the largest specific surface area of 370.75 $m^2\ g^{-1}$, which could provide enormous active sites for

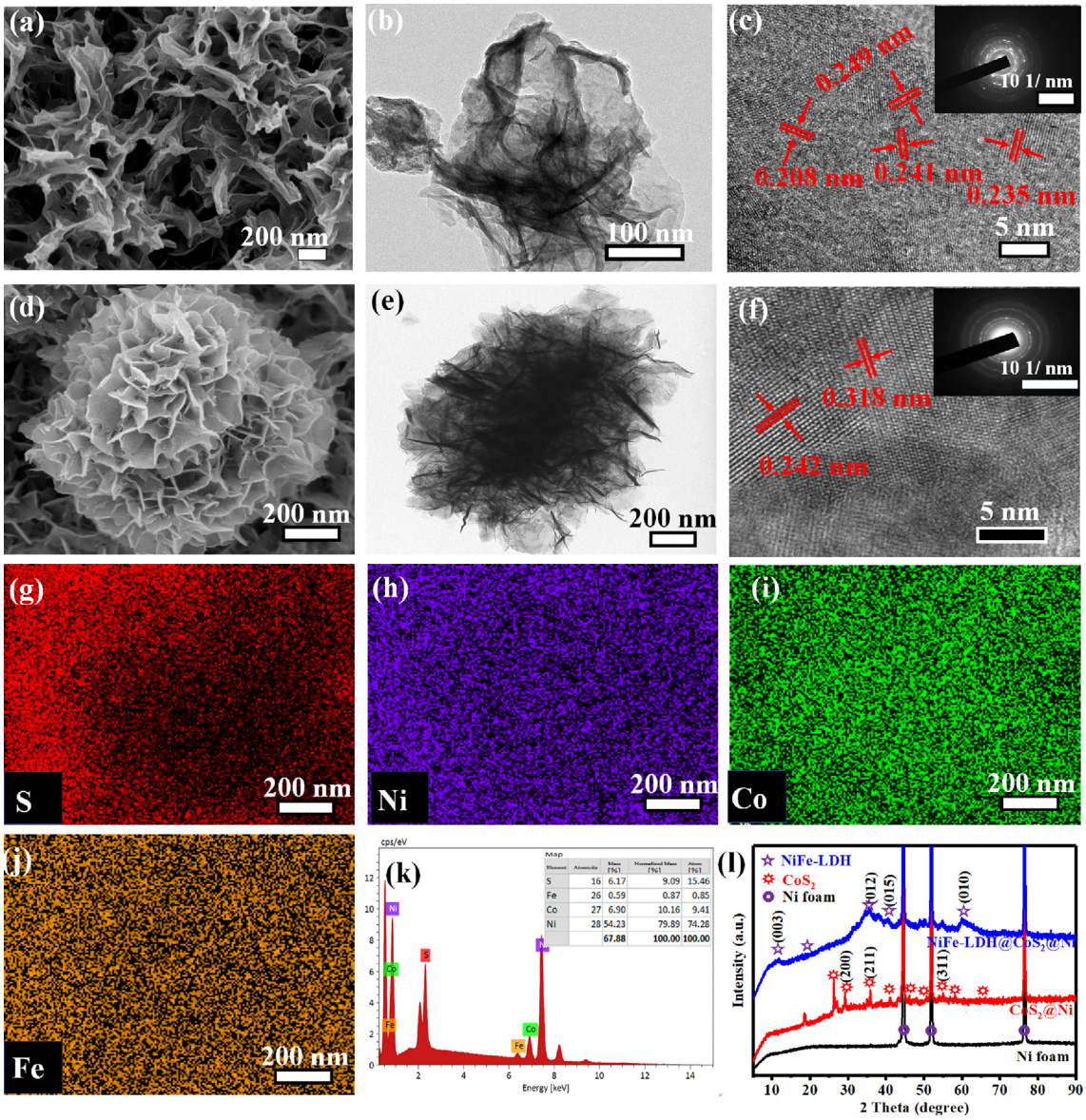

Fig. 2. (a) SEM image, (b) TEM image and (c) HRTEM image of as-prepared CoS_2@Ni nanosheets and their corresponding SAED image (inset of Fig. 2c). The EDX elemental mapping images (g-j) for S, Ni, Co and Fe elements of NiFe-LDH@CoS_2@Ni and its corresponding SEM images (d). (e) TEM image and (f) HRTEM image of as-prepared NiFe-LDH@CoS_2@Ni and its corresponding SAED image (inset of Fig. 2f). (k) EDX spectrum of NiFe-LDH@CoS_2@Ni. (l) XRD patterns of NiFe-LDH@CoS_2@Ni, CoS_2@Ni and Ni foam.

achieving outstanding electrochemical performance. Therefore, we selected 10 h as the optimal experimental condition. Additionally, the SEM images of NiFe-LDH@Ni are displayed in Fig. S5, and the XRD pattern and N_2 adsorption–desorption isotherm, as well as their pore size distributions of NiFe-LDH@Ni, are shown in Fig. S6. The surface area of NiFe-LDH@Ni was found to be 270 $m^2\ g^{-1}$.

The electrochemical characteristics of the as-prepared CoS_2@Ni, NiFe-LDH@Ni and NiFe-LDH@CoS_2@Ni electrodes were evaluated. Fig. 5a-c depicts the cyclic voltammetry (CV) curves of CoS_2@Ni, NiFe-LDH@Ni and NiFe-LDH@CoS_2@Ni electrodes at different scans from 10 to 100 mV s^{-1}. Sure enough, a pair of Faradaic redox peaks were observed in the voltage window of 0–0.7 V, which should result from the reversible redox properties of Ni^{2+}/Fe^{3+} and Fe^{2+}/Fe^{3+} [46]. The shape of the CV curves showed the capacitance characteristic with the obvious redox peaks, implying that the capacitance of the fabricated electrode mainly derived from faradaic redox reactions. More importantly, the NiFe-LDH@CoS_2@Ni electrode showed a larger specific capacitance than CoS_2@Ni (Fig. 5a) and NiFe-LDH@Ni (Fig. 5b) electrodes under the same scan rates, which may be on account of the enormous active sites supplied by ultrathin nanosheets and implies the better capacitive properties of the NiFe-LDH@CoS_2@Ni electrode. In addition, Fig. 5g shows the CVs of all fabricated electrodes at a constant scan rate of 50 mV s^{-1}. The largest CV curve area of NiFe-LDH@CoS_2@Ni electrode can be observed among the tested electrodes, illustrating the highest capacitance characteristic and the fastest redox reaction kinetic process, respectively.

In addition, GCD curves of NiFe-LDH@Ni and NiFe-LDH@CoS_2@Ni electrodes were also measured at different current density (Fig. 5d–f). The discharge time of NiFe-LDH@CoS_2@Ni electrode was the longest compared to those of CoS_2@Ni and NiFe-LDH@Ni electrodes, indicating the stable performance for the charge storage. Meanwhile, the GCD curve of the NiFe-LDH@CoS_2@Ni electrode was almost symmetric in shape, indicating high coulombic efficiency. Furthermore, the

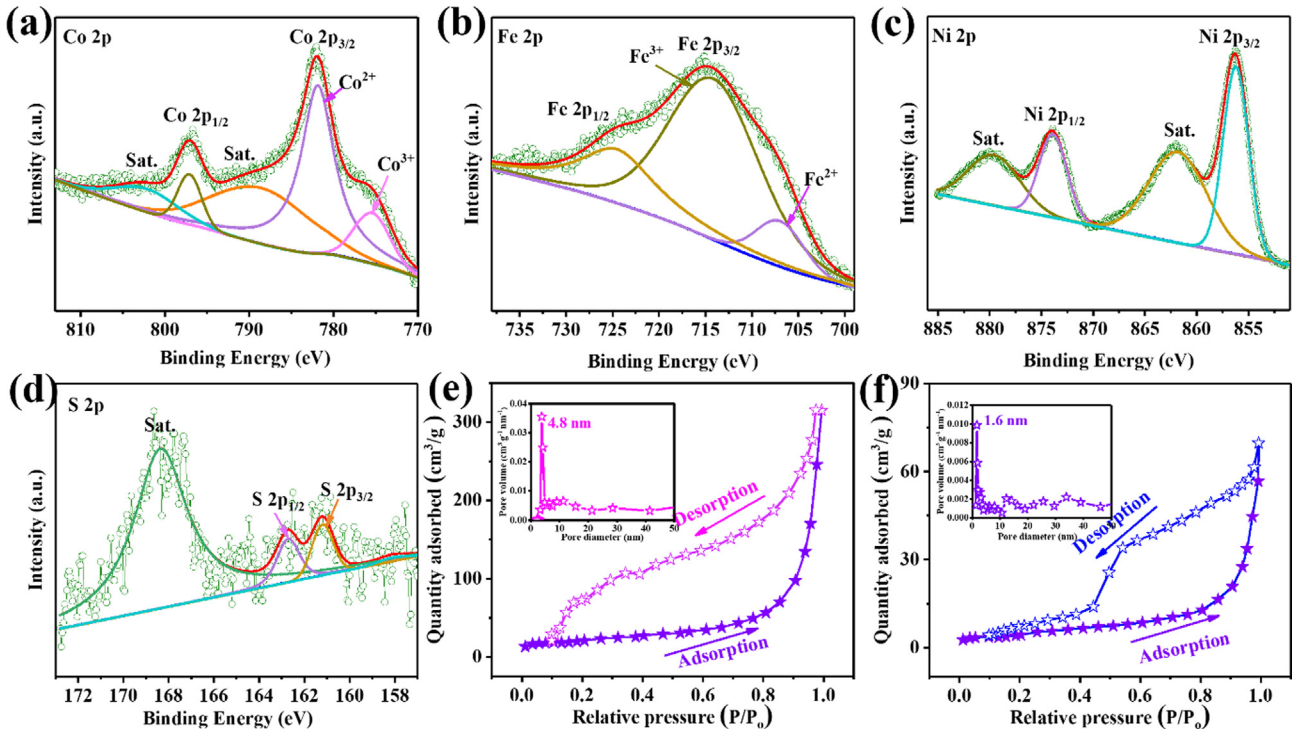

Fig. 3. (a) Narrow scan spectra for Co 2p (a), Fe 2p (b), Ni 2p (c) and S 2p (d) of NiFe-LDH@CoS_2@Ni respectively. N_2 adsorption-desorption isotherm of (e) NiFe-LDH@CoS_2@Ni and (f) CoS_2@Ni and their pore size distributions (insets of Fig. 3e and f), respectively.

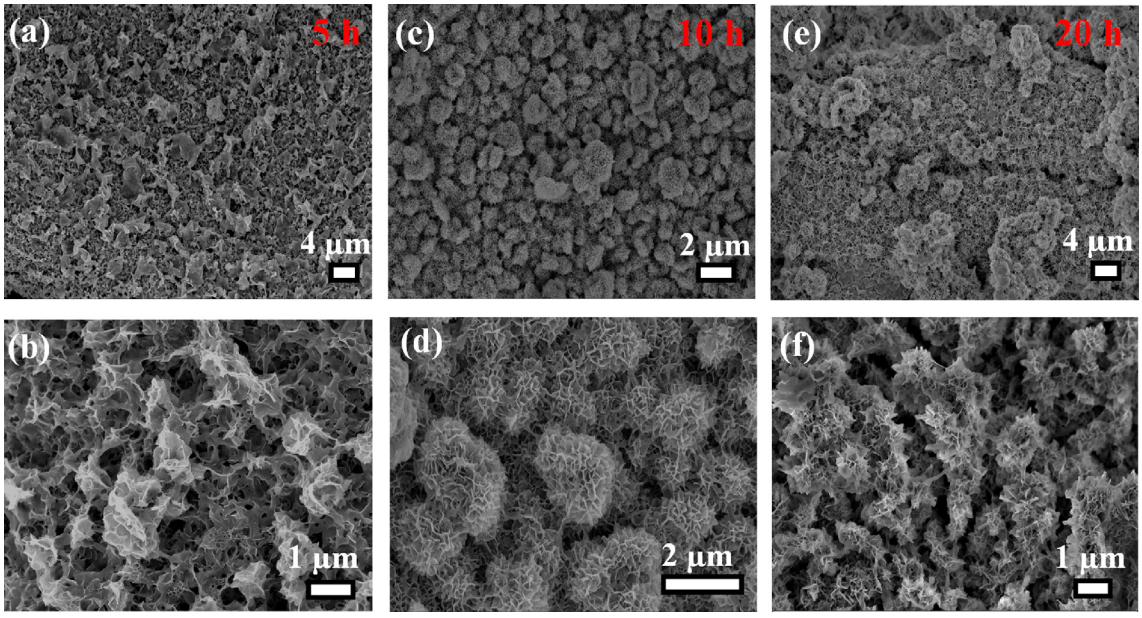

Fig. 4. SEM images of NiFe-LDH samples obtained at different growth time: 5 h (a-b), 10 h (c-d) and 20 h (e-f), respectively.

NiFe-LDH@CoS_2@Ni electrode showed much longer discharge time than other precursor electrodes at 5 mA cm^{-2}, which was consistent with the CV results (Fig. 5h and g). Additionally, other electrodes also exhibited a gradually decreased discharge time with the increasing current density range from 2 to 20 mA cm^{-2}, which indicated the excellent reversible performance during the charge–discharge process (Fig. 5d–f). The areal capacitance of NiFe-LDH@CoS_2@Ni calculated by Eq. (1) is 11.28 F cm^{-2} at 2 mA cm^{-2}, while the areal capacitances of CoS_2@Ni and NiFe-LDH@Ni were calculated to be 5.712 and 0.864 F cm^{-2} at the same current density, respectively. Additionally, the calculated specific capacitance of CoS_2@Ni, NiFe-LDH@Ni and NiFe-LDH@CoS_2@Ni based on the discharge time is exhibited in Fig. 5j. It can be found that the flower-like structured electrode achieved the highest capacitance, indicating that the advanced flower-like structure can provide the largest specific surface area and the best electrochemical performance. Furthermore, CoS_2@Ni, NiFe-LDH@Ni and NiFe-LDH@CoS_2@Ni electrodes were also measured by EIS in frequencies ranging from 100 kHz to 0.01 Hz and the Nyquist plots are shown in Fig. 5i, the Nyquist plots of these electrodes all containing a

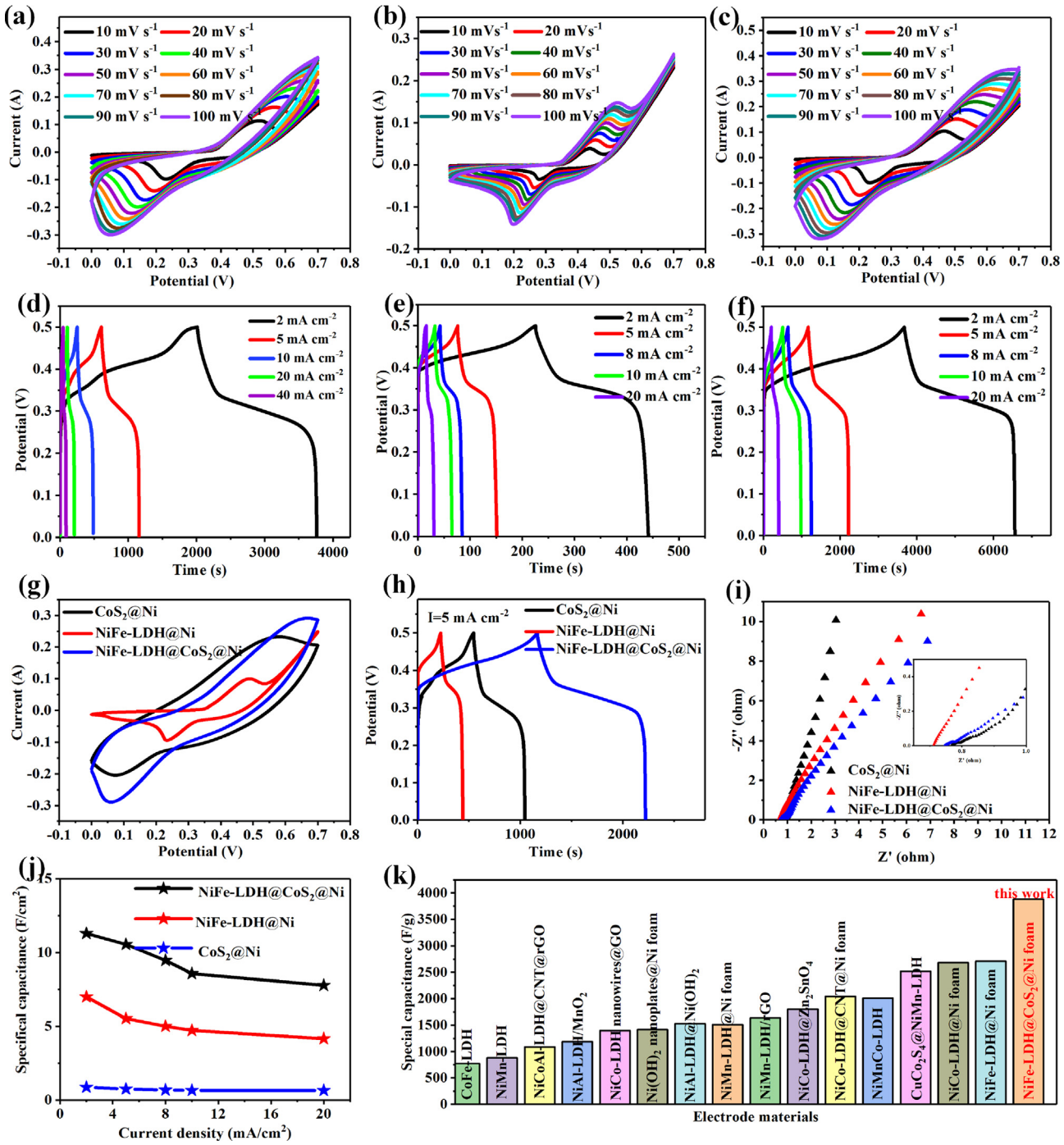

Fig. 5. Electrochemical performance measurements in three-electrode system. (a-c) CV curves of CoS_2@Ni, NiFe-LDH@Ni and NiFe-LDH@CoS_2@Ni electrodes at different scan rates, respectively. (d-f) GCD curves of CoS_2@Ni, NiFe-LDH@Ni and NiFe-LDH@CoS_2@Ni electrodes at different current densities, respectively. (g) CV curves of the CoS_2@Ni, NiFe-LDH@Ni and NiFe-LDH@CoS_2@Ni electrodes measured at the scan rate of 50 mV s^{-1}. (h) GCD curves of the CoS_2@Ni, NiFe-LDH@Ni and NiFe-LDH@CoS_2@Ni electrodes measured at 5 mA cm^{-2}. (i) Nyquist plots of the CoS_2@Ni, NiFe-LDH@Ni and NiFe-LDH@CoS_2@Ni electrodes in the frequency range from 100 kHz to 0.01 Hz with an amplitude of 5 mV, respectively. The inset shows the plots in high-frequency range. (j) Specific capacitance of CoS_2@Ni, NiFe-LDH@Ni and NiFe-LDH@CoS_2@Ni at different current densities. (k) Comparison of the electrochemical performance of NiFe-LDH@CoS_2@Ni with those different LDH-based electrode materials reported.

semicircle and a straight line can be seen. The semicircle line corresponds to charge-transfer resistance (R_{ct}) at high frequency and the straight line presents ion diffusion resistance at low frequency [47,48]. At high frequency, the intrinsic resistance of the electrode materials, the ionic resistance of the electrolyte and the contact resistance at the active material/current collector interface are associated with the equivalent internal resistance Rs (the intercept at the X-axis). As shown in the inset of Fig. 5i, the Rs values of CoS_2@Ni, NiFe-LDH@Ni and NiFe-LDH@CoS_2@Ni electrodes were measured to be 0.77 Ω, 0.71 Ω and 0.74 Ω, respectively. The lower Rs value of NiFe-LDH@CoS_2@Ni electrode indicated the NiFe-LDH@CoS_2@Ni electrode material had low internal impedance and excellent conductivity.

As shown in Fig. 5k, the prepared electrode based on the flower-like structured composites achieved a better capacitance compared with the LDH-based electrodes previously reported. Cycling

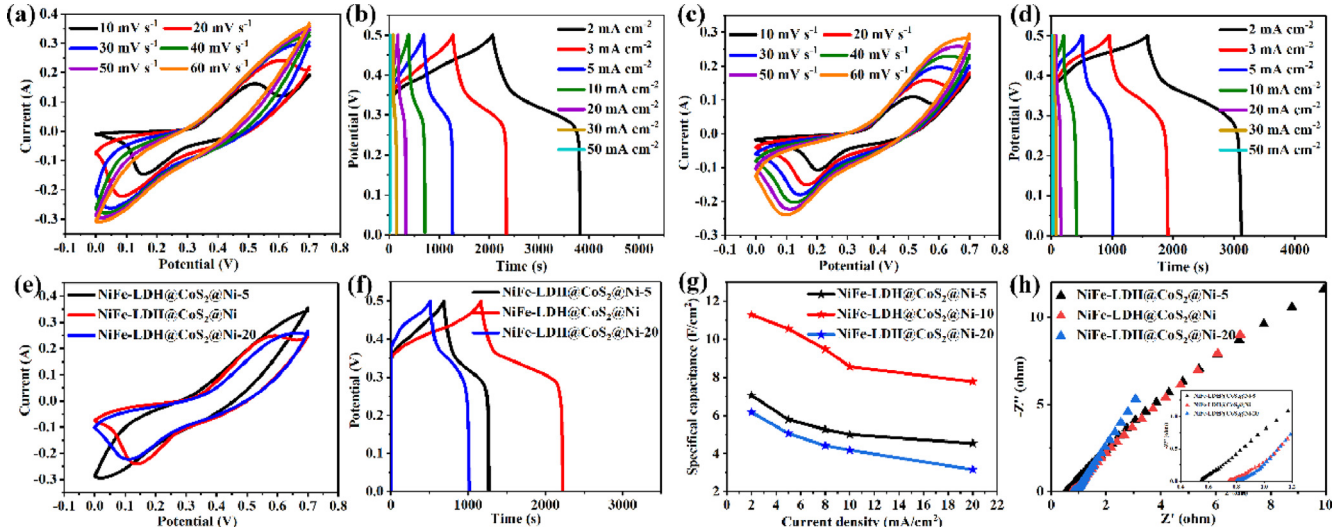

Fig. 6. Electrochemical performance measurements in three-electrode system. (a, c) CV curves of NiFe-LDH@CoS_2@Ni-5 and NiFe-LDH@CoS_2@Ni-20 electrodes at different scan rates, respectively. (b, d) GCD curves of NiFe-LDH@CoS_2@Ni-5 and NiFe-LDH@CoS_2@Ni-20 electrodes at different current densities, respectively. (e) CV curves of the NiFe-LDH@CoS_2@Ni-5, NiFe-LDH@CoS_2@Ni and NiFe-LDH@CoS_2@Ni-20 electrodes measured at a scan rate of 50 mV s^{-1}. (f) GCD curves of the NiFe-LDH@CoS_2@Ni-5, NiFe-LDH@CoS_2@Ni and NiFe-LDH@CoS_2@Ni-20 electrodes measured at 5 mA cm^{-2}. (g) Specific capacitance of NiFe-LDH@CoS_2@Ni-5, NiFe-LDH@CoS_2@Ni and NiFe-LDH@CoS_2@-Ni-20 at different current densities. (h) Nyquist plots of the NiFe-LDH@CoS_2@Ni-5, NiFe-LDH@CoS_2@Ni and NiFe-LDH@CoS_2@Ni-20 electrodes in the frequency range from 100 kHz to 0.01 Hz with an amplitude of 5 mV, respectively. The inset shows the plots in high-frequency range.

performance and coulombic efficiency of the NiFe-LDH@CoS_2@Ni electrode measured at 20 mA cm^{-2} and the SEM image of NiFe-LDH@CoS_2@Ni after 10,000 electrochemical cycles are shown in Fig. S8. The fabricated NiFe-LDH@CoS_2@Ni electrode presented a good stability and 81.9% of capacitance was still maintained after 10,000 electrochemical cycles. Moreover, the coulombic efficiency of NiFe-LDH@CoS_2@Ni was measured to be about 81.3% after 10,000 electrochemical cycles as shown in Fig. S8 [20,49,50]. The SEM image of NiFe-LDH@CoS_2@Ni after 10,000 electrochemical cycles has no obvious change as shown in the inset of Fig. S8. Additionally, the TEM image, XRD pattern and EDX elemental mapping images of NiFe-LDH@CoS_2@Ni after 10,000 electrochemical cycles and its corresponding SEM images are also displayed in Fig. S9. It can be seen that the flower-like structure still kept the basic structure. The XRD spectrum of CoS_2@Ni shows three diffraction bands of (200), (211) and (311), which confirm the stability of CoS_2 [51]. From NiFe-LDH@CoS_2@Ni, the diffraction planes of (003), (006) and (012) confirm the formation of LDH materials, which are all in accord with the diffraction planes of the sample before 10,000 electrochemical cycles [52]. The remarkable electrochemical performance of NiFe-LDH@CoS_2@Ni hybrid can be attributed to the following superiorities: Firstly, the CoS_2 nanosheets directly grown on the conductive Ni foam, so as to provide excellent conductivity to the electrode; secondly, the ultra-thin nanosheets of NiFe-LDH are interconnected, can not only support a large surface area but also provide abundant active sites for electrochemical reactions during the charging-discharging process; thirdly, the porous nanospheres structure provides effective channels for electrolyte ions diffusion which can accelerate the transfer rate of electrolyte ions, resulting in the enhanced electrochemical performance. All of these advantages endow the NiFe-LDH@CoS_2@Ni with excellent capacitive performance.

The electrochemical characteristics of NiFe-LDH@CoS_2@Ni-5 and NiFe-LDH@CoS_2@Ni-20 were also evaluated in a three-electrode in 6 M KOH aqueous electrolyte. Fig. 6a and c depict the cyclic voltammetry (CV) curves of NiFe-LDH@CoS_2@Ni-5 and NiFe-LDH@CoS_2@Ni-20 electrodes at different scan rates from 10 to 100 mV s^{-1} respectively. Compared with NiFe-LDH@CoS_2@Ni-5 and NiFe-LDH@CoS_2@Ni-20, NiFe-LDH@CoS_2@Ni (Fig. 5c) showed a larger CV curve area and more pronounced redox peak at high current densities, which may be due to the abundant active sites and large specific surface area supplied by ultrathin nanosheets. In addition, GCD curves of NiFe-LDH@CoS_2@Ni-5 and NiFe-LDH@CoS_2@Ni-10 electrodes were also measured at different current densities (Fig. 6b and d). The areal capacitance of NiFe-LDH@CoS_2@Ni-5 and NiFe-LDH@CoS_2@Ni-20 was calculated to be 7.053 and 6.173 F cm^{-2} at a current density of 2 mA cm^{-2}, respectively. Also, Fig. 6e shows the CVs of all fabricated electrodes at a constant scan rate of 50 mV s^{-1}. The largest CV curve area of NiFe-LDH@CoS_2@Ni electrode can be observed among the tested electrodes, illustrating the highest capacitance characteristic and the fastest redox reaction kinetic process. As shown in Fig. 6f, it can be observed that the discharge time of NiFe-LDH@CoS_2@Ni electrode was the longest, indicating the greatest ability for charge storage [53,54]. Additionally, the calculated specific capacitances of NiFe-LDH@CoS_2@Ni-5, NiFe-LDH@CoS_2@Ni and NiFe-LDH@CoS_2@Ni-20 based on the discharge time are exhibited in Fig. 6g. It can be found that the electrode of NiFe-LDH@CoS_2@Ni achieved the highest capacitance, indicating that the special flower-like structure can provide the largest specific surface area and the best electrochemical performance. The NiFe-LDH@CoS_2@Ni-5, NiFe-LDH@CoS_2@Ni and NiFe-LDH@CoS_2@Ni-20 electrodes were also measured by EIS in frequencies ranging from 100 kHz to 0.01 Hz and the Nyquist plots are shown in Fig. 6h. The Rs values of NiFe-LDH@CoS_2@Ni-5, NiFe-LDH@CoS_2@Ni and NiFe-LDH@CoS_2@Ni-20 electrodes were measured to be 0.54 Ω, 0.74 Ω and 0.80 Ω, respectively.

To further evaluate the energy storage performance of the NiFe-LDH@CoS_2@Ni electrode for practical applications, an asymmetric all-solid-state supercapacitor (ASC) device was successfully assembled using the NiFe-LDH@CoS_2@Ni composite as the positive electrode and AC as the negative electrode (NiFe-LDH@CoS_2@Ni//AC). The individual CV curves of AC and NiFe-LDH@CoS_2@Ni electrodes tested at a sweep rate of 50 mV s^{-1} in a voltage window from 0 to 0.7 V and −1 to 0 V in 6 M KOH electrolyte were shown in Fig. 7a, Fig. 7b and c show the CV and GCD curves of the NiFe-LDH@CoS_2@Ni//AC ASC device measured in different voltage windows at a scan rate of 50 mV s^{-1} and a current density of 1 A

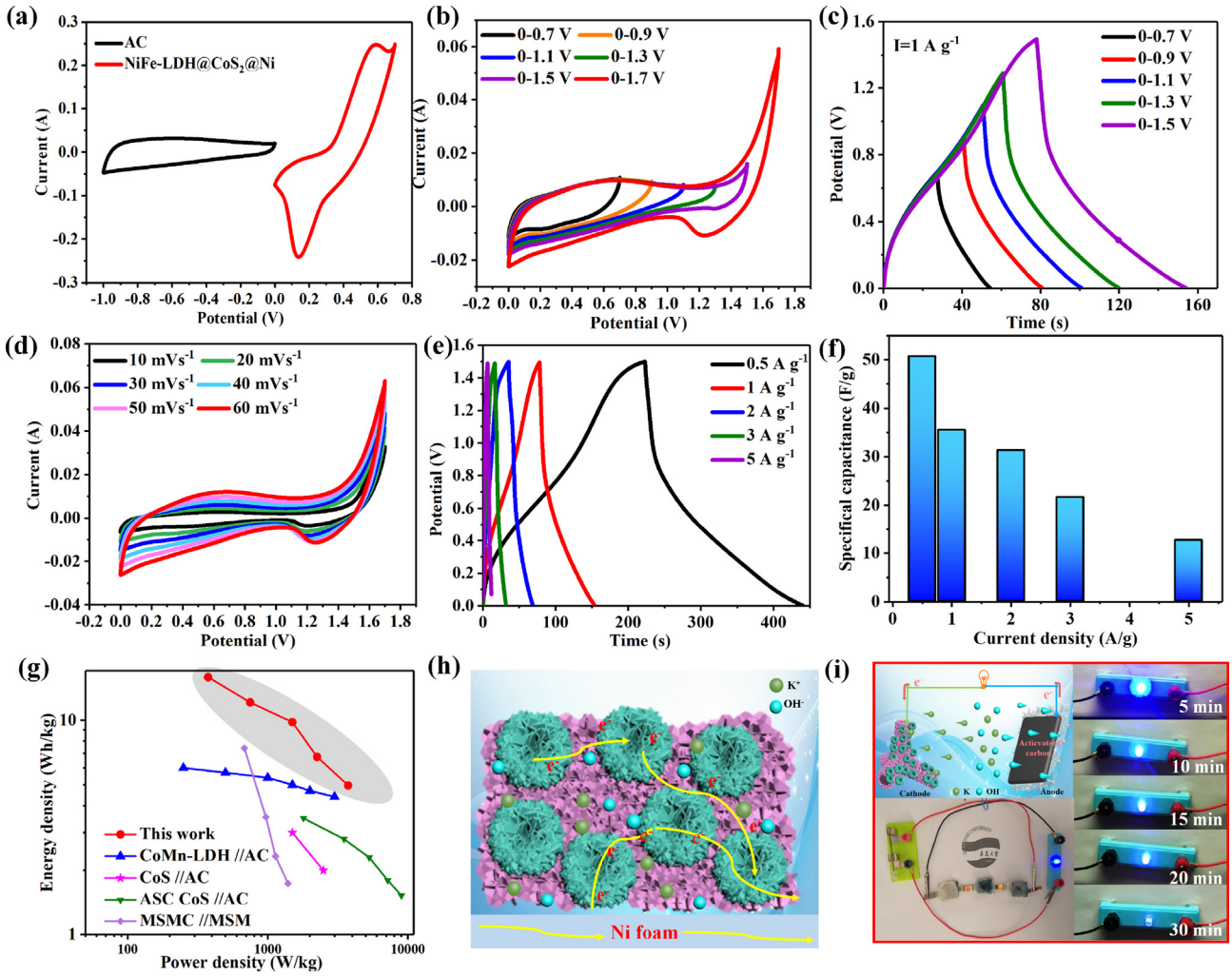

Fig. 7. (a) CV curves of AC and NiFe-LDH@CoS_2@Ni electrodes measured at a sweep rate of 50 mV s^{-1} in a three-electrode system, respectively. (b) CV curves of NiFe-LDH@CoS_2@Ni//AC ASC measured at a sweep rate of 50 mV s^{-1} in different potential windows. (c) GCD curves of NiFe-LDH@CoS_2@Ni//AC ASC measured in different potential windows at 1 A g^{-1}. (d) CV curves of NiFe-LDH@CoS_2@Ni//AC ASC at different scan rates. (e) GCD curves of NiFe-LDH@CoS_2@Ni//AC ASC at different current densities. (f) Histogram of specific capacitance of ASC devices at various current densities. (g) Ragone plot of the as-fabricated NiFe-LDH@CoS_2@Ni//AC asymmetric supercapacitor device and those recently reported from literature. (h) Schematic of electron transportation of NiFe-LDH@CoS_2@Ni. (i) The schematic configuration of the NiFe-LDH@CoS_2@Ni//AC ASC device and corresponding photographs of three ASC devices connected in series which could light up LEDs.

g^{-1}, respectively. The shape of the CV curves remained the same in different potential windows when the operating voltage was extended to 1.7 V. Moreover, the shapes of all GCD curves also remained the same in different potential windows, which proved the excellent capacitance performance. Fig. 7d shows the CV curves of the ASC device measured in a potential window of 0–1.7 V at different scan rates ranging from 10 to 60 mV s^{-1}. The GCD curves of NiFe-LDH@CoS_2@Ni//AC ASC device at different current densities from 0.5 to 5 A g^{-1} are displayed in Fig. 7e. The NiFe-LDH@CoS_2@Ni//AC ASC device exhibits a specific capacitance of 51.4 F g^{-1} at 0.5 A g^{-1} and maintains 14.8 F g^{-1} at 5 A g^{-1} as displayed in Fig. 7f, revealing its good rate capability. The remarkable supercapacitor performance for NiFe-LDH@CoS_2@Ni can be mainly attributed to the convenient channels for electron transportation, as shown in Fig. 7h. The CoS_2 nanosheets do not only act as active electrode material in the electrochemical reaction but also as a framework to support the NiFe-LDH@CoS_2@Ni flower-like nanospheres. The NiFe-LDH@CoS_2@Ni flower-like nanospheres with abundant active sites and large specific surface area could provide convenient channels and low the internal resistance for electron transportation. The excellent supercapacitor performance of NiFe-LDH@CoS_2@Ni indicates promising energy storage applications. As shown in Fig. 7g, the as-fabricated device presents an energy density of 15.84 Wh kg^{-1} at a power density of 375.16 W kg^{-1}, which is comparable with some recently reported devices, such as CoMn-LDH //AC (5.9 Wh kg^{-1} at 250 W kg^{-1}, 4.4 Wh kg^{-1} at 2500 W kg^{-1}) [55], ASC CoS//AC (5.3 Wh kg^{-1} at 1800 W kg^{-1}, 1.53 Wh kg^{-1} at 9000 W kg^{-1}) [56], MSMC//MSM (7.41 Wh kg^{-1} at 681 W kg^{-1}, 1.74 Wh kg^{-1} at 1396 W kg^{-1}) [57]. Furthermore, an all-solid-state ASC device of NiFe-LDH@CoS_2@Ni//AC was assembled with KOH/poly(vinyl alcohol) (PVA) as the gel electrolyte to assess its practical application. As shown in Fig. 7i, a blue LED indicator with a working voltage of 2.5 V can be lighted for more than 30 min when three ASC devices are connected in series.

4. Conclusions

In conclusion, the NiFe-LDH@CoS_2@Ni flower-like structure on 3D porous Ni foam was successfully achieved by the facile two-step hydrothermal methods and directly used to fabricate a binder-free electrode with an excellent specific capacitance of 11.28 F cm^{-2} (3880 F g^{-1}) at 2 mA cm^{-2} (1.17 A g^{-1}). In addition, an all-solid-state asymmetric supercapacitor was also fabricated by NiFe-LDH@CoS_2@Ni hybrid and presented a high energy density

of 15.84 Wh kg^{-1} at the power density of 375.16 W kg^{-1} that can light up a blue LED indicator for 30 min. The remarkable electrochemical performances can be ascribed to the flower-like structure of ultra-thin nanosheet, which provides high specific surface area and a large number of active sites, shortens the diffusion distance between electrolyte ions and substrates and accelerates the electron transport. Therefore, this study confirms that the NiFe-LDH@CoS_2@Ni hybrid has great potential as electrode materials for high-performance supercapacitors.

CRediT authorship contribution statement

Jinmi Tian: Investigation, Methodology, Writing-original draft. **Aitang Zhang:** Conceptualization, Resources, Writing-review & editing. **Rui Liu:** Data curation. **Weiguo Huang:** Data curation. **Zhen Yuan:** Supervision. **Rongkun Zheng:** Supervision. **Di Wei:** Supervision. **Jingquan Liu:** Conceptualization, Project administration, Funding acquisition.

Declaration of Competing Interest

The authors declare that they have no known competing financial interests or personal relationships that could have appeared to influence the work reported in this paper.

Acknowledgments

This work was supported by Qingdao Innovation Leading Talent Program, Taishan Scholars Program and Shandong Provincial Natural Science Foundation (ZR2018BEM020).

Appendix A. Supplementary data

Supplementary data to this article can be found online at https://doi.org/10.1016/j.jcis.2020.06.086.

References

[1] K.C. Ho, L.Y. Lin, A review of electrode materials based on core-shell nanostructures for electrochemical supercapacitors, J. Mater. Chem. A 7 (2019) 3516–3530.
[2] Y.W. Shi, X.X. Wang, J.L. Luo, Q. Xie, Fabrication and characterization of polyoxometalate/2D graphene-based flexible supercapacitors for wearable electronic pulse-beat application, J. Mater. Sci.: Mater. Electron. 30 (2019) 3692–3700.
[3] G. Xiong, P. He, D. Wang, Q. Zhang, T. Chen, T.S. Fisher, Hierarchical Ni-Co hydroxide petals on mechanically robust graphene petal foam for high-energy asymmetric supercapacitors, Adv. Funct. Mater. 26 (2016) 5460–5470.
[4] J. Xu, Z.Q. Tan, W.C. Zeng, G.X. Chen, S.L. Wu, Y. Zhao, K. Ni, Z.C. Tao, M. Ikram, H.X. Ji, Y.W. Zhu, A hierarchical carbon derived from sponge-templated activation of graphene oxide for high-performance supercapacitor electrodes, Adv. Mater. 28 (2016) 5222–5228.
[5] B. Mendoza-Sã, Y. Gogotsi, Synthesis of two-dimensional materials for capacitive energy storage, Adv. Mater. 28 (2016) 6104–6135.
[6] S.H. Lee, K.J. Chang, G.T. Hwang, K.J. Lee, Self-powered flexible inorganic electronic system, Nano Energy 14 (2015) 111–125.
[7] J. Yan, W. Qian, W. Tong, Z. Fan, Supercapacitors: recent advances in design and fabrication of electrochemical supercapacitors with high energy densities, Adv. Energy Mater. 4 (2014).
[8] X. Xi, D. Wu, L. Han, Y. Yu, R. Liu, Highly uniform carbon sheets with orientation-adjustable ordered mesopores, ACS Nano 12 (2018).
[9] P. Simon, Y. Gogotsi, Materials for electrochemical capacitors, Nat. Mater. 7 (2008) 845–854.
[10] P. Chang, K. Matsumura, J. Zhang, J. Qi, C. Wang, T. Kinumoto, T. Tsumura, M. Chen, M. Toyoda, 2D porous carbon nanosheets constructed of few-layer graphene sheets by "medium-up" strategy for ultrahigh power-output EDLCs, J. Mater. Chem. A (2018) 10.1039.C1038TA02308E.
[11] A.G. Kannan, A. Samuthirapandian, D.W. Kim, Electric double-layer capacitors employing nitrogen and sulfur co-doped, hierarchically porous graphene electrodes with synergistically enhanced performance, J. Power Sources 337 (2017) 65–72.
[12] L. Jiang, L. Sheng, C. Xu, W. Tong, Z. Fan, Construction of nitrogen-doped porous carbon building by interconnected ultra-small carbon nanosheets for ultra-high rate supercapacitors, J. Mater. Chem. A 4 (2016).
[13] Y. Liu, N. Fu, G. Zhang, M. Xu, W. Lu, L. Zhou, H. Huang, Design of hierarchical Ni Co@Ni Co layered double hydroxide core-shell structured nanotube array for high-performance flexible all-solid-state battery-type supercapacitors, Adv. Funct. Mater. 27 (2017) 1605307.
[14] G. Nagaraju, R. Kakarla, S.M. Cha, J.S. Yu, Highly flexible conductive fabrics with hierarchically nanostructured amorphous nickel tungsten tetraoxide for enhanced electrochemical energy storage, Nano Res. 8 (2015) 3749–3763.
[15] H.N. Jia, Z.Y. Wang, X.H. Zheng, Y.F. Cai, J.H. Lin, H.Y. Liang, J.L. Qi, J. Cao, J.C. Feng, W.D. Fei, Controlled synthesis of MOF-derived quadruple-shelled CoS_2 hollow dodecahedrons as enhanced electrodes for supercapacitors, Electrochim. Acta 312 (2019) 54–61.
[16] B. You, N. Li, H.Y. Zhu, X.L. Zhu, J. Yang, Graphene oxide-dispersed pristine CNTs support for MnO_2 nanorods as high-performance supercapacitor electrodes, ChemSusChem 6 (2013) 474–480.
[17] B. You, P.Q. Yin, L.N. An, Multifunctional electroactive heteroatom-doped carbon aerogels, Small 10 (2014) 4352–4361.
[18] C.L. Zheng, J.L. Zhang, Q. Zhang, B. You, G.L. Chen, Three dimensional Ni foam-supported graphene oxide for binder-free pseudocapacitor, Electrochim. Acta 152 (2015) 216–221.
[19] X. Liu, B. You, X.Y. Yu, J. Chipman, Y.J. Sun, Electrochemical oxidation to construct a nickel sulfide/oxide heterostructure with improvement of capacitance, J. Mater. Chem. A 4 (2016) 11611–11615.
[20] B. You, Y.J. Sun, Hierarchically porous nickel sulfide multifunctional superstructures, Adv. Energy Mater. 6 (2016) 1502333.
[21] M. Jin, S.Y. Lu, L. Ma, M.Y. Gan, Y. Lei, X.L. Zhang, G. Fu, P.S. Yang, M.F. Yan, Different distribution of in-situ thin carbon layer in hollow cobalt sulfide nanocages and their application for supercapacitors, J. Power Sources 341 (2017) 294–301.
[22] Q. Pan, Y.H. Liu, L.J. Zhao, Co_9S_8/Mo_2S_3 nanorods on CoS_2 laminar arrays as advanced electrode with superior rate properties and long cycle life for asymmetric supercapacitors, Chem. Eng. J 351 (2018) 603–612.
[23] L. Zhang, H.B. Wu, X.W. Lou, David, Unusual CoS_2 ellipsoids with anisotropic tube-like cavities and their application in supercapacitors, Chem. Commun. 48 (2012) 6912–6914.
[24] R.C. Jin, L.X. Yang, G.H. Li, G. Chen, Hierarchical worm-like CoS_2 composed of ultrathin nanosheets as an anode material for lithium-ion batteries, J. Mater. Chem. A 3 (2015) 10677–10680.
[25] X. Li, D. Du, Z. Yu, X. Wei, Q. Xue, Z.F. Yan, Layered double hydroxides toward high-performance supercapacitors, J. Mater. Chem. A 5 (2017).
[26] Y.F. Zhao, Q. Wang, T. Bian, H.J. Yu, H. Fan, C. Zhou, L.Z. Wu, C.H. Tung, D. O'Hare, T. Zhang, Ni^{3+} doped monolayer layered double hydroxide nanosheets as efficient electrodes for supercapacitors, Nanoscale 7 (2015) 7168–7173.
[27] L.J. Xie, Z.A. Hu, C.X. Lv, G.H. Sun, J.L. Wang, Y.Q. Li, H.W. He, W. Jian, K.X. Li, Co_xNi_{1-x} double hydroxide nanoparticles with ultrahigh specific capacitances as supercapacitor electrode materials, Electrochim. Acta 78 (2012) 205–211.
[28] F.L. Lai, Y.P. Huang, Y.E. Miao, T.X. Liu, Controllable preparation of multi-dimensional hybrid materials of nickel-cobalt layered double hydroxide nanorods/nanosheets on electrospun carbon nanofibers for high-performance supercapacitors, Electrochim. Acta 174 (2015) 456–463.
[29] J. Yang, C. Yu, X. Fan, J. Qiu, Supercapacitors: 3D architecture materials made of NiCoAl-LDH Nanoplates Coupled with NiCo-carbonate hydroxide nanowires grown on flexible graphite paper for asymmetric supercapacitors, Adv. Energy. Mater.
[30] C.H. Bai, S.G. Sun, Y.Q. Xu, R.J. Yu, H.J. Li, Facile one-step synthesis of nanocomposite based on carbon nanotubes and Nickel-Aluminum layered double hydroxides with high cycling stability for supercapacitors, J. Colloid Interface Sci. 480 (2016) 57–62.
[31] L. Min, Z. Ming, Q.W. Zhong, X.Z. Yu, Flower-like NiFe layered double hydroxides coated MnO_2 for high-performance flexible supercapacitors, J. Energy Storage 11 (2017) 242–248.
[32] L.G. Xiao, Y.L. Xiao, D.H. Xiao, J.Z. Shi, D. Fan, Q.W. Zhong, X.Z. Yu, Nickel-manganese layered double hydroxide nanosheets supported on nickel foam for high-performance supercapacitor electrode materials, Electrochim. Acta 194 (2016) 179–186.
[33] S. Tajik, D.P. Dubal, P. Gomez-Romero, A. Yadegari, A. Rashidi, B. Nasernejad, A. M. Asiri Inamuddin, Nanostructured mixed transition metal oxides for high performance asymmetric supercapacitors: facile synthetic strategy, J. Hydrogen Energy (2017).
[34] V. Singh, A. Tiwari, T.C. Nagaiah, Facet-controlled morphology of cobalt disulfide towards enhanced oxygen reduction reaction, J. Mater. Chem. A 6 (2018) 22545–22554.
[35] Y. Lu, B. Jiang, L. Fang, F.L. Ling, F. Wu, B.S. Hu, F.M. Meng, K.Y. Niu, F. Lin, H.M. Zheng, An investigation of ultrathin nickel-iron layered double hydroxide nanosheets grown on nickel foam for high-performance supercapacitor electrodes, J. Alloys Compd. 714 (2017) 63–70.
[36] Z. Wenwen, S. Shiguo, X. Yongqian, Y. Ruijin, L. Hongjuan, Facile synthesis of NiAl-LDH/MnO2 and NiFe-LDH/MnO2 composites for high-performance asymmetric supercapacitors, J. Alloys Compd.
[37] X.M. Li, J.T. Zai, Y.Y. Liu, X.B. He, S.J. Xiang, Z.F. Ma, X.F. Qian, Atomically thin layered NiFe double hydroxides assembled 3D microspheres with promoted electrochemical performances, J. Power Sources 325 (2016) 675–681.
[38] S.P. Wang, J. Wu, J.W. Yin, Q. Hu, D.S. Geng, L.M. Liu, Improved electrocatalytic performance in overall water splitting with rational design of hierarchical Co_3O_4@NiFe-LDH core-shell nanostructure on Ni foam, ChemElectroChem 5 (2018) 1357–1363.

[39] A.M.P. Sakita, E. Vallés, R.D. Noce, A.V. Benedetti, Novel NiFe/NiFe-LDH composites as competitive catalysts for clean energy purposes, Appl. Surf. Sci. 447 (2018) 107–116.
[40] J. Liu, J.S. Wang, B. Zhang, Y.J. Ruan, L. Lv, X. Ji, K. Xu, L. Miao, J.J. Jiang, Hierarchical $NiCo_2S_4$@NiFe LDH heterostructures supported on nickel foam for enhanced overall-water-splitting activity, ACS Appl. Mater. Interfaces 9 (2017) 15364–15372.
[41] Y.M. Bi, Z. Cai, D.J. Zhou, Y. Tian, Q. Zhang, Q. Zhang, Y. Kuang, Y. Li, X.M. Sun, X. Duan, Understanding the incorporating effect of Co^{2+}/Co^{3+} in NiFe-layered double hydroxide for electrocatalytic oxygen evolution reaction, J. Catal. 358 (2018) 100–107.
[42] C. Zhang, M.F. Shao, L. Zhou, Z.H. Li, K.M. Xiao, M. Wei, Hierarchical NiFe layered double hydroxide hollow microspheres with highly-efficient behavior toward oxygen evolution reaction, ACS Appl. Mater. Inter. 8 (2016) 33697–33703.
[43] G. Abellán, E. Coronado, C.J. Gómez-García, C. Martí-Gastaldo, A. Ribera, Intercalation of cobalt(II)-tetraphenylporphine tetrasulfonate complex in magnetic NiFe-layered double hydroxide, Polyhedron 52 (2013) 216–221.
[44] B. Wang, J. Park, D. Su, C. Wang, H. Ahn, G. Wang, Solvothermal synthesis of CoS_2–graphene nanocomposite material for high-performance supercapacitors, J. Mater. Chem. 22 (2012) 15750–15756.
[45] J.C. Xing, Y.L. Zhu, Q.W. Zhou, X.D. Zheng, Q.J. Jiao, Fabrication and shape evolution of CoS_2 octahedrons for application in supercapacitors, Electrochim. Acta 136 (2014) 550–556.
[46] T.R. Zhan, Y.M. Zhang, X.L. Liu, S.S. Lu, W.G. Hou, NiFe layered double hydroxide/reduced graphene oxide nanohybrid as an efficient bifunctional electrocatalyst for oxygen evolution and reduction reactions, J. Power Sources 333 (2016) 53–60.
[47] W. Huang, A. Zhang, H. Liang, R. Liu, J. Cai, L. Cui, J. Liu, Novel fabrication of hollow and spinous $NiCo_2S_4$ nanotubes templated by natural silk for all-solid-state asymmetric supercapacitors, J. Colloid Interface Sci. 549 (2019) 140–149.
[48] R. Liu, A.T. Zhang, J.G. Tang, J.M. Tian, W.G. Huang, J.T. Cai, C. Barrow, W.R. Yang, J.Q. Liu, Fabrication of cobaltosic oxide nanoparticle-doped 3 D MXene/graphene hybrid porous aerogels for all-solid-state supercapacitors, Chem. Eur. J. 25 (2019) 5547–5554.
[49] B. You, Y.J. Sun, Innovative strategies for electrocatalytic water splitting, Accounts Chem. Res. 51 (2018) 1571–1580.
[50] X. Liu, B. You, Y.J. Sun, Facile surface modification of ubiquitous stainless steel led to competent electrocatalysts for overall water splitting, ACS Sustain. Chem. Eng. 5 (2017) 4778–4784.
[51] M. Govindasamy, S. Shanthi, E. Elaiyappillai, S.-F. Wang, P.M. Johnson, H. Ikeda, Y. Hayakawa, S. Ponnusamy, C. Muthamizhchelvan, Fabrication of hierarchical $NiCo_2S_4$@CoS_2 nanostructures on highly conductive flexible carbon cloth substrate as a hybrid electrode material for supercapacitors with enhanced electrochemical performance, Electrochim. Acta 293 (2019) 328–337.
[52] B. You, X. Liu, N. Jiang, Y.J. Sun, A general strategy for decoupled hydrogen production from water splitting by integrating oxidative biomass valorization, J. Am. Chem. Soc. 138 (2016) 13639–13646.
[53] T. Xiao, S.L. Wang, J. Li, N. Yang, W. Li, P. Xiang, L.H. Jiang, X.Y. Tan, Sulfidation of NiFe-layered double hydroxides as novel negative electrodes for supercapacitors with enhanced performance, J. Alloys Compd. 768 (2018) 635–643.
[54] Y. Ma, Y.C. Wang, D.H. Xie, Y. Gu, H.M. Zhang, G.Z. Wang, Y.X. Zhang, H.J. Zhao, P.K. Wong, NiFe-layered double hydroxide nanosheet arrays supported on carbon cloth for highly sensitive detection of nitrite, ACS Appl. Mater. Inter. 10 (2018) 6541–6551.
[55] A.D. Jagadale, G.Q. Guan, X.M. Li, X. Du, X. Ma, X.G. Hao, A. Abudula, Ultrathin nanoflakes of cobalt–manganese layered double hydroxide with high reversibility for asymmetric supercapacitor, J. Power Sources 306 (2016) 526–534.
[56] K. Subramani, N. Sudhan, R. Divya, M. Sathish, All-solid-state asymmetric supercapacitors based on cobalt hexacyanoferrate-derived CoS and activated carbon, RSC Adv. 7 (2017) 6648–6659.
[57] S.S. Karade, B.R. Sankapal, Two dimensional cryptomelane like growth of $MoSe_2$ over MWCNTs: symmetric all-solid-state supercapacitor, J. Electroanalytical Chem. 802 (2017) 131–138.